Journal of Hazardous Materials 188 (2011) 422–427

Contents lists available at ScienceDirect

Journal of Hazardous Materials

journal homepage: www.elsevier.com/locate/jhazmat

Removal of oxygenated volatile organic compounds by catalytic oxidation over Zr–Ce–Mn catalysts

Saïd Azalim[a,b], Manuel Franco[a], Rachid Brahmi[b], Jean-Marc Giraudon[a], Jean-François Lamonier[a,*]

[a] Univ Lille Nord de France, USTL, Unité de Catalyse et de Chimie du Solide, UMR CNRS 8181, 59652 Villeneuve d'Ascq, France
[b] UCD, Laboratoire de Catalyse et de Corrosion des Matériaux, Faculté des Sciences, 24000 El Jadida, Morocco

ARTICLE INFO

Article history:
Received 1 October 2010
Received in revised form
28 December 2010
Accepted 31 January 2011
Available online 26 February 2011

Keywords:
VOC
Catalytic oxidation
Zr–Ce–Mn mixed oxides
Butanol

ABSTRACT

The composition–activity relationship of Zr–Ce–Mn–O materials was investigated for the catalytic removal of Oxygenated Volatile Organic Compounds (OVOC) emitted by stationary sources. Using a sol–gel method, very high surface specific areas, small crystallite sizes and high redox properties were obtained for $Zr_{0.4}Ce_{0.6-x}Mn_xO_2$ catalytic systems after calcination at 500 °C. The textural and redox properties were improved when Mn content increased in the material, especially for $x = 0.36$. As a result the most active and selective catalyst in the butanol (model of OVOC) oxidation was obtained for the nominal composition $Zr_{0.4}Ce_{0.24}Mn_{0.36}O_2$ due to a high oxygen mobility and surface Mn^{4+} concentration.

© 2011 Elsevier B.V. All rights reserved.

1. Introduction

Volatile organic compounds (or VOCs) are major air pollutants and their treatment by catalytic oxidation is one of the most promising ways to reduce these pollutants. This technique has the advantage of operating at low temperatures (200–500 °C), thus leading to low NOx formation. Noble-metal oxide catalysts using supported Pt or Pd are conventionally used [1,2]. However, attention has also been given to transition metals due to the limited availability and high cost of noble metals [3,4]. To improve the performance of transition metal oxide catalysts, the dispersion of active metallic species must be optimized by using a suitable support [5] and/or a synergistic effect between different species must be achieved through the formation of mixed oxides. Among the transition metal oxides, mixed-valent manganese oxide materials are good candidates for oxygenated VOC removal. The γ-MnO_2 phase has been reported to be more active than β-MnO_2 or Mn_2O_3 in the oxidation of ethanol [6]. In the same reaction, K–oxides (cryptomelane type) are also reported because of the presence of Mn^{4+}/Mn^{3+} ions and the hydrophobic character of the solid [7]. Due to the favorable properties of ceria in oxidation catalysis, the Mn–Ce–O catalytic system has also been examined in the VOC removal by catalytic wet or dry oxidation [8–11]. MnO_x–CeO_2 mixed oxides had much higher catalytic activity than that of pure MnO_x and CeO_2 owing to the formation of the solid solution between manganese and cerium oxides [12]. But the interactions between MnO_x and CeO_2 vary with the composition and the optimum Mn/Ce ratio depends on (i) the catalyst synthesis method and (ii) the nature of the pollutant to be destroyed. Besides it is well known that formation of mixed oxides of ceria with Zr^{4+} enhanced oxygen storage properties of ceria and the so-formed mixed oxides exhibited good thermal stability [13].

Butanol enters the environment from either natural sources or during its production, transport, storage and use as a chemical intermediate and a solvent. The primary route for entering the environment is the release to the atmosphere when used as a solvent for paints, coatings, varnishes, resins, gums, vegetable oils, etc. Occupational exposure may occur through inhalation and dermal contact with this compound at workplaces where n-butanol is produced or used. n-Butanol is not classifiable as to human and animal carcinogenicity [14]. However a 10 year study, conducted of men exposed to this compound (>200 ppm of n-butanol) in an industrial setting, revealed ocular symptoms included a burning sensation, blurring of vision, lachrymation, and photophobia [15]. Animal exposed to n-butanol in air may manifest ataxia, central nervous system depression, prostration. Deaths from acute overexposure are believed due to respiratory failure. Guinea pigs exposed to 100 ppm, (4 h/day; 6 day/week for 64 exposures) showed a decrease in number of red blood count. Rats subjected to 130 h of total exposure to a concentration of 8000 ppm showed CNS depression [15].

In spite of numerous studies covering catalytic oxidation of a wide range of VOCs, only few reports deal with catalytic total

* Corresponding author. Fax: +33 320436561.
E-mail address: jean-francois.lamonier@univ-lille1.fr (J.-F. Lamonier).

0304-3894/$ – see front matter © 2011 Elsevier B.V. All rights reserved.
doi:10.1016/j.jhazmat.2011.01.135

oxidation of n-butanol in air, in order to remove this hazardous compound [16–18]. Papaefthimiou et al. [16,17] have studied the oxidation of a VOC mixture which includes ethyl acetate, benzene and n-butanol. Butanol has been chosen as representative model compounds for alcohols. The main scope of this work was to determine the most active group VIII metal catalysts for the removal of this VOC mixture. Among them Pt and Pd supported on alumina [16] and titania [17] were the most active metals for benzene and butanol oxidation. V_2O_5–WO_3/TiO_2 catalyst, recognized as combining high activity and selectivity together with a strong stability in Cl_2–HCl environments, has been studied in the oxidation of various compounds by Everaert and Baeyens [18]. This work is mainly focused on chlorinated VOC but butanol oxidation experiment has also been performed and the activation energy for the butanol is done in comparison with other VOC in the presence of V_2O_5–WO_3/TiO_2 catalyst

The present work describes different Zr–Ce–Mn–O catalytic systems synthesized using a sol–gel method. Generally the sol–gel method has been recognized as an interesting way to prepare catalysts with the control of their texture, composition, homogeneity and structural properties [19]. The focus is to optimize the performances of the Zr–Ce–Mn oxides for complete oxidation of n-butanol by examining the effect of Mn amount.

2. Experimental

The mixed metal oxides catalysts $Zr_{0.4}Ce_{0.6-x}Mn_xO_2$ ($x = 0$; 0.12; 0.24; 0.36; 0.48; 0.60) were prepared using a sol–gel method. The $ZrO(NO_3)_2{\cdot}5H_2O$, $Ce(NO_3)_3{\cdot}6H_2O$ and $Mn(NO_3)_2{\cdot}5H_2O$ (0.5 mol/L) nitrates were dissolved separately in ethanol and then mixed together in the desired molar ratio of Zr:Ce:Mn. The resulting solution was heated at 80 °C and deionized water containing 5 vol.% of ethanol was added to it under constant stirring. The resulting gel was gradually formed after few minutes and the temperature was maintained for 1.5 h. The gel was then allowed to mature overnight at room temperature (RT) before being heated at 80 and 100 °C, respectively, in order to remove ethanol and excess water. After grinding, the resulting powders were calcined by heating from RT to 300 °C (2 h) and from 300 to 500 °C (2 h) in flowing air.

The powder X-ray diffraction patterns (XRD) of the samples were collected with a D8 Advance-BRUKER diffractometre using Cu Kα radiation. The diffractograms were recorded with the 2θ range of 10–80° with a step size of 0.02° and a step time of 2 s. The average crystallite size was determined from the Scherrer equation. The lattice parameter was estimated using FullProf software. The nitrogen adsorption and desorption isotherms were measured at −196 °C on a Micromeritics ASAP 2010 apparatus. The samples were degassed at 160 °C for 4 h before the measurement. The specific surface area was calculated using the BET model. H_2-temperature programmed reduction (H_2-TPR) was investigated (Micromeritics Autochem II) by heating the samples (50 mg) in H_2 (5 vol.%)/Ar flow (50 mL min^{-1}) at a heating rate of 5 °C min^{-1} from 20 to 900 °C.

X-ray photoelectron spectroscopy (XPS) analyses were conducted with Kratos Axis Ultra DLD spectrometer with a monochromatic Al Kα ($h\nu = 1486.6$ eV) radiation source operated at 15 kV and 15 mA. The binding energy (BE) was calibrated based on the line position of C 1s (285 eV). CasaXPS processing software was used to estimate the relative abundance of the different species.

The activity of the catalysts (200 mg) was measured in a continuous flow system on a fixed bed reactor at atmospheric pressure and space velocity of 12,000 h^{-1}. The flow (100 mL min^{-1}) of the reactant gases (800 ppm of butanol in air) was adjusted by a Calibrage PUL 010 and DGM 110 apparatus comprising of a saturator and one mass flow controller. The reactor temperature was increased from RT to 400 °C (0.5 °C min^{-1}). The exit gases were analyzed by a VARIAN 3800 gas chromatograph equipped with a FID for the analysis of the organic reactants and a TCD for the analysis of CO and CO_2.

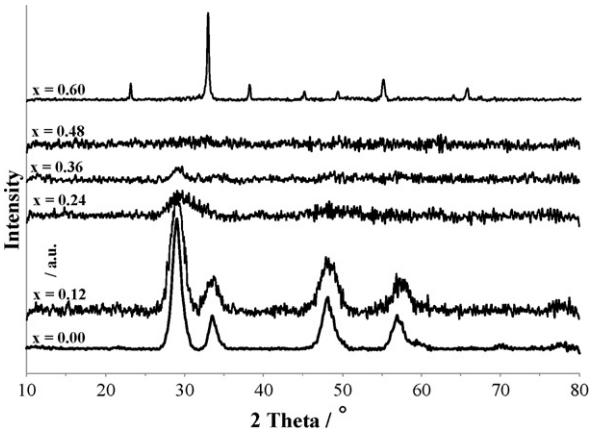

Fig. 1. XRD patterns of $Zr_{0.4}Ce_{0.6-x}Mn_xO_2$ solids.

3. Results and discussion

XRD patterns of $Zr_{0.4}Ce_{0.6-x}Mn_xO_2$ samples are displayed in Fig. 1. The pattern of $Zr_{0.4}Ce_{0.6}O_2$ can be satisfactorily indexed in a fluorite type of structure [20], suggesting the Zr ions incorporation in the cubic lattice to form a homogeneous Zr–Ce–O solid solution. The cubic lattice has been confirmed by Raman spectroscopy. Indeed a strong broad band centered at 480 cm^{-1} and attributed to the Raman-active F_{2g} mode has been observed for $Zr_{0.4}Ce_{0.6}O_2$ sample (not shown). Decrease in the lattice parameter a from 5.4120 Å for pure CeO_2 [21] to 5.315 (±0.001)Å is observed on the calcined $Zr_{0.4}Ce_{0.6}O_2$ sample, in accordance with the smaller ionic radius of Zr^{4+} ion (0.84 Å) compared to that of Ce^{4+} (0.97 Å). When adding small amounts of manganese, the fluorine-type structure is preserved (Fig. 1). No manganese and zirconium oxide phases are detected on $Zr_{0.4}Ce_{0.48}Mn_{0.12}O_2$ solid. The absence of such phases suggests that Mn and Zr related species may be incorporated into the CeO_2 lattice forming solid solutions [22]. This is also supported by the lower value of the lattice constant a of $Zr_{0.4}Ce_{0.48}Mn_{0.12}O_2$ sample (5.303 ± 0.001 Å) due to the low ionic radius of Mn^{n+} (Mn^{2+} = 0.83 Å, Mn^{3+} = 0.64 Å, and Mn^{4+} = 0.53 Å). Only a broad asymmetric peak in the 2θ range of 25–35° is observed for the $Zr_{0.4}Ce_{0.36}Mn_{0.24}O_2$ sample with a higher Mn content. As the Mn content is further increased, ($Zr_{0.4}Ce_{0.24}Mn_{0.36}O_2$) the same peak is less obvious and appears significantly enlarged. Finally the most enriched Mn sample containing cerium is totally amorphous. Hence with increasing content of manganese in the presence of cerium, amorphous nature of the samples is enhanced. Similar qualitative observations have been reported on Mn–Ce–O composites elsewhere [22,23]. These authors attribute this to the occurrence of more defective fluorite like lattices having a lower degree of crystallinity and a smaller particle size as the sample is enriched with Mn. Compared to Ce–Mn–O systems, the greater degree of amorphous nature in this study could be due to presence of zirconium which retards the crystallization of the samples and/or allows forming some small oxide related crystallites. The XRD pattern of $Zr_{0.4}Mn_{0.6}O_2$ is constituted of peaks attributed to Mn_2O_3 phase (JCPDS 41-1442) without any ZrO_2 crystallization.

The addition of Mn to the Zr–Ce–O system leads to increase in surface area and a corresponding increase and decrease in porous volume and crystallite size respectively as shown in Table 1. The specific surface area doubles on increasing x from 0 to 0.48; the average crystallite size which is 4.5 nm for $x = 0$ decreases to 1.2 nm

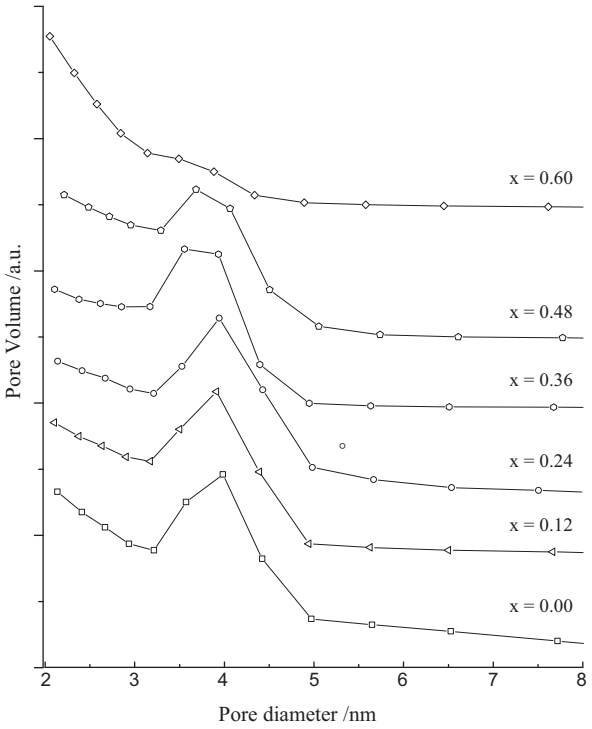

Fig. 2. Pore size distribution of $Zr_{0.4}Ce_{0.6-x}Mn_xO_2$ solids.

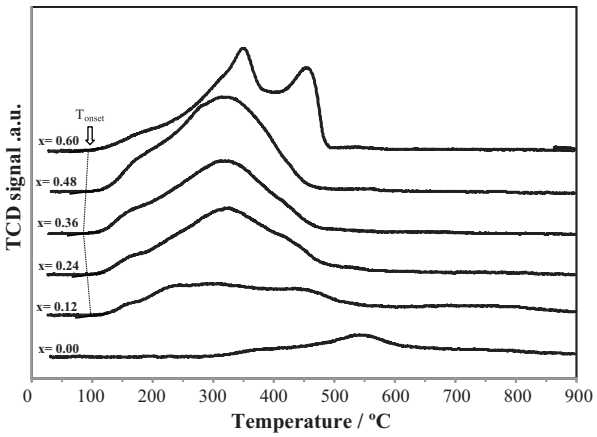

Fig. 3. H_2-TPR of $Zr_{0.4}Ce_{0.6-x}Mn_xO_2$ solids.

for $x = 0.36$. For $x = 0.60$, an Mn_2O_3 average crystallite size of 30 nm is measured, the corresponding high specific area can be explained by the formation of amorphous zirconia. Similar systems with nominal composition $Zr_{0.3}Ce_{0.6}Mn_{0.1}O_2$ have been synthesized by a sol–gel method using citric acid as chelating agent [9,24]. Specific surface area of 55 $m^2\,g^{-1}$ has been obtained by the authors after a calcination step at 500 °C. Then a much higher surface area (>110 $m^2\,g^{-1}$) can be reached using our synthesis procedure. Fig. 2 displays the porous diameter distribution for $Zr_{0.4}Ce_{0.6-x}Mn_xO_2$ samples. A porous diameter distribution centered on 4 nm is found whatever the x value and is stressed for the cerium containing samples. Similar correlation between the BET surface area and average pore radius has been obtained by Fornasiero et al. [20]: for a half specific area (50 $m^2\,g^{-1}$ for $Ce_{0.6}Zr_{0.4}O_2$ mixed oxides prepared by citrate method), a double average pore diameter size (8 nm) has been found.

Fig. 3 shows the H_2-TPR profiles of $Zr_{0.4}Ce_{0.6-x}Mn_xO_2$ samples. H_2-TPR profile of $Zr_{0.4}Ce_{0.6}O_2$ exhibits a main reduction peak centered at 543 °C related to the concomitantly reduction of Ce^{4+} ions at the surface and in the bulk of the overall solid solution. The presence in the TPR profile of the shoulder at around 370 °C may be related to the presence of some ceria impurity not incorporated in the solid solution [25]. H_2-TPR curve of $Zr_{0.4}Mn_{0.6}O_2$ shows two overlapped strong reduction peaks at 351 and 454 °C. Assuming that +II is the final reduction state of manganese species, the peak at low temperature can be ascribed to the reduction of Mn_2O_3 to Mn_3O_4. The peak at high temperature corresponds to the reduction of Mn_3O_4 to MnO. Addition of cerium to Zr–Mn solid shifts the reduction temperature of manganese and cerium species to lower temperature. The promotion in the temperature reduction points to the interaction between manganese and cerium species. From $x = 0$ to $x = 0.36$, the reduction onset temperature decreases (Fig. 3), indicating an increase in the oxygen mobility. From $x = 0.36$ to $x = 0.60$, a decrease in oxygen mobility is observed (Table 1 and Fig. 3). Similar results on mesoporous MnO_x–CeO_2 samples have been observed by Zou et al. [26] and an optimum Mn/Ce ratio of 0.67 has been reported. The total H_2 consumption is listed in Table 1. Assuming that both Mn^{n+} species are reduced completely to Mn^{2+}, Zr^{4+} is not reduced in the temperature range studied, and Ce^{3+}/Ce^{4+} bulk molar ratio is unchanged, an average oxidation number (AON) of manganese is obtained for each sample (Table 1). AON value of 3 for $Zr_{0.4}Mn_{0.6}O_2$ matches well with the Mn_2O_3 phase identified by XRD. AON values >3.2 indicate the presence of Mn^{3+} and Mn^{4+} species mixture in the Zr–Ce–Mn solids.

The surface XPS values of Ce/(Ce + Mn), calculated from the area of the Ce 3d and Mn 2p core levels, are lower than the bulk ratio expected for the $Zr_{0.4}Ce_{0.12}Mn_{0.48}O_2$ sample (Table 2). This can be explained by the formation of manganese-rich oxide phase at the surface. This result has already been observed in Mn–Ce systems [26]. An example of the XPS spectra of Mn 2p, Mn 3s, O 1s and Ce 3d is depicted in Fig. 4. The O 1s core-level spectra have been fitted with two peak contributions, referred to as O_I and O_{II} components (Fig. 4). The major peak O_I with BE of 529.5–529.9 eV is characteristic of lattice oxygen [27,28]. This component O_I is displaced towards higher BE with Mn content increase (Table 2) due to higher BE of lattice oxygen in MnO_x than in CeO_2 [27]. Component O_{II} with BE of 531.2 eV belongs probably to defect oxide, hydroxyl or carbonate groups [28]. The relative abundance of these two kinds of oxygen species is similar for all compositions ($O_I \sim 63\%$ and $O_{II} \sim 37\%$). The Mn 3 s peak splitting widths for different Mn oxides are helpful to find out the oxidation state of manganese species [29,30], an Mn

Table 1
Textural and redox properties of $Zr_{0.4}Ce_{0.6-x}Mn_xO_2$ samples.

Samples	Average crystallite size (nm)	Specific surface area ($m^2\,g^{-1}$)	V_p ($cm^3\,g^{-1}$)	H_2 consumption ($\mu mol\,g^{-1}$)	Onset temperature (°C)	Average oxidation number of Mn
$Zr_{0.4}Ce_{0.6}O_2$	4.5	98	0.087	957	280	–
$Zr_{0.4}Ce_{0.48}Mn_{0.12}O_2$	2.8	110	0.084	1700	93	3.8
$Zr_{0.4}Ce_{0.36}Mn_{0.24}O_2$	1.2	157	0.124	2423	82	3.7
$Zr_{0.4}Ce_{0.24}Mn_{0.36}O_2$	1.2	163	0.130	2880	80	3.4
$Zr_{0.4}Ce_{0.12}Mn_{0.48}O_2$	–	199	0.146	3467	90	3.2
$Zr_{0.4}Mn_{0.60}O_2$	30.6	167	0.093	3579	86	3.0

Table 2
Data obtained from XPS analyses of $Zr_{0.4}Ce_{0.6-x}Mn_xO_2$ samples.

Samples	$(Ce/(Ce+Mn))_{Bulk}$	$(Ce/(Ce+Mn))_{XPS}$	O 1s BE (eV)		ΔE Mn 3s (eV)	% u‴	Mn 2p	
			O_I	O_{II}			% Mn^{3+}	% Mn^{4+}
$Zr_{0.4}Ce_{0.6}O_2$	1.00	1.00	529.5	531.2	–	14	–	
$Zr_{0.4}Ce_{0.48}Mn_{0.12}O_2$	0.79	0.60	529.6	531.2	5.2	16	66	34
$Zr_{0.4}Ce_{0.36}Mn_{0.24}O_2$	0.58	0.42	529.7	531.2	5.1	15	64	36
$Zr_{0.4}Ce_{0.24}Mn_{0.36}O_2$	0.45	0.28	529.8	531.2	5.1	13	60	40
$Zr_{0.4}Ce_{0.12}Mn_{0.48}O_2$	0.19	0.19	529.8	531.4	5.1	11	60	40
$Zr_{0.4}Mn_{0.60}O_2$	–	–	529.9	531.5	5.4	–	100	–

3s splitting width ΔE of 4.8 and 5.4 eV correspond to the presence of Mn^{4+} and Mn^{3+}, respectively. Therefore, Mn^{4+} and Mn^{3+} ions are certainly present together at the surface, since an Mn 3s splitting width ΔE of 5.1–5.2 eV is observed in all the Ce containing samples (Table 2). This is in agreement with an AON > 3.2 calculated from the H_2-TPR data. Mn 3 s splitting width ΔE of 5.4 eV is observed in $Zr_{0.4}Mn_{0.6}O_2$, indicating that Mn^{3+} is exclusively formed at the surface when cerium element is absent. This correlates with Mn_2O_3 formation observed in XRD analysis. The BE of Mn $2p_{3/2}$ photopeak is rather broad and the co-existence of Mn^{4+} and Mn^{3+} at the surface can be suggested (Fig. 4). Mn $2p_{3/2}$ peak can be split in two components which give reasonable fitting with BE of 643.4 and 641.8 eV for Mn^{4+} and Mn^{3+}, respectively. These values are found to be higher than those recorded from pure MnO_2 and Mn_2O_3, probably due the strong interaction between manganese, cerium and zirconium oxides. Clearly with increasing Mn, the relative concentration of Mn^{4+} increases from 34% to 40% (Table 2). The same observation has been reported on MnO_x–CeO_2 mixed oxides [8]. The Ce 3d spectra of Ce^{4+} and Ce^{3+} can be resolved into six and four components, respectively [31]. The Ce $3d_{5/2}$ BE in ceria is found close to 882.0 eV. Addition of zirconium and manganese to ceria causes an upper shift of 0.3–0.4 eV which can be considered as a direct evidence for solid solution formation. The relative abundance of Ce^{4+} present in the solid is assessed through the calculation of the percentage of the area under the Ce^{4+} u‴ (916.7 eV) relative to the total area under the Ce 3d spectral envelop using the method proposed by Shyu et al. [32]. Addition of a small amount of Mn causes an increase in the surface Ce^{4+} concentration since u‴ intensity goes from 14% to 16%. But with further Mn content increase, the concentration of Ce^{4+} decreases (Table 2). This result can be explained by an electrons transfer from Mn to Ce, since in parallel, Mn^{4+} concentration increases. In Mn–Ce–O composites, Chen et al. [23] suggested an electron transfer but from Ce to Mn since addition of manganese to cerium increased the abundance of surface Ce^{4+} species.

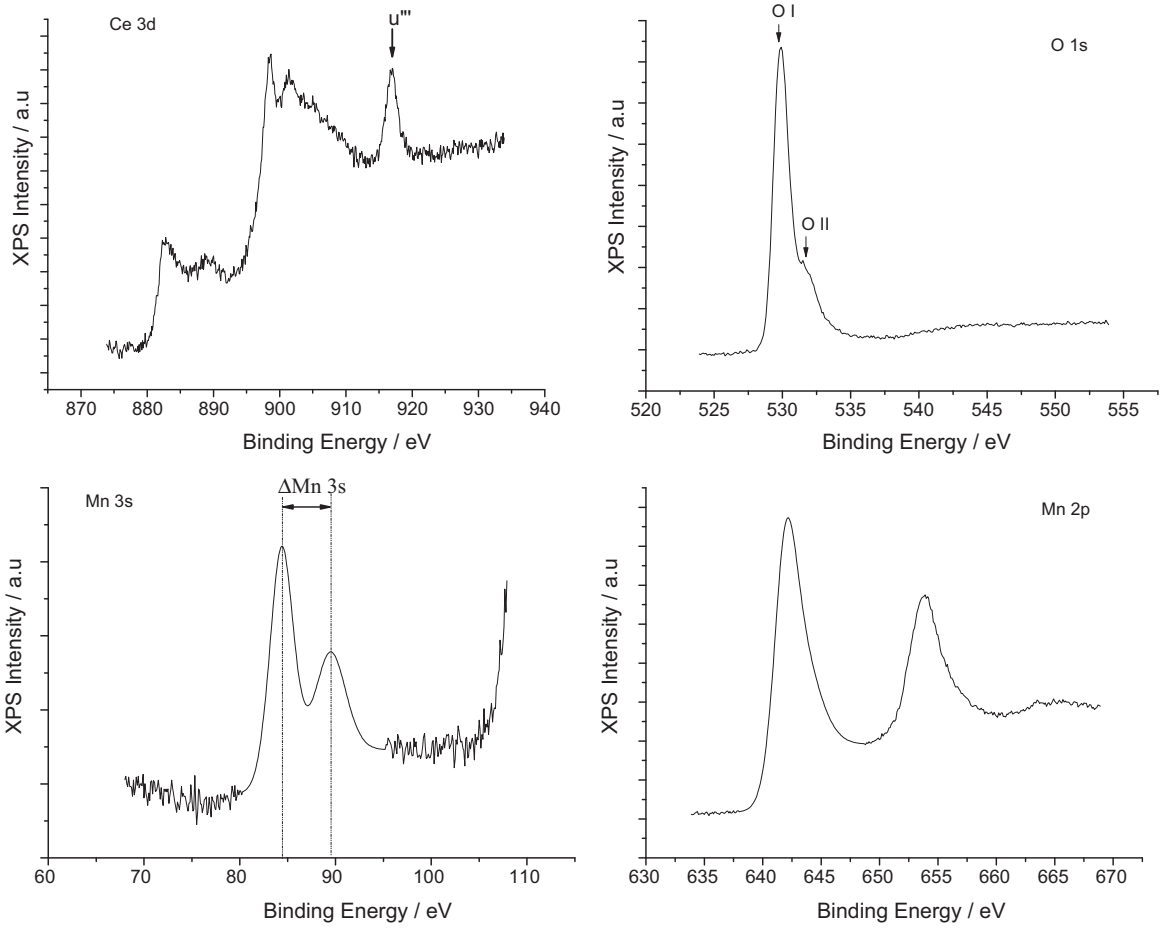

Fig. 4. XPS spectra of Ce 3d, O 1s, Mn 2p and Mn 3s core levels in $Zr_{0.40}Ce_{0.12}Mn_{0.48}O_2$.

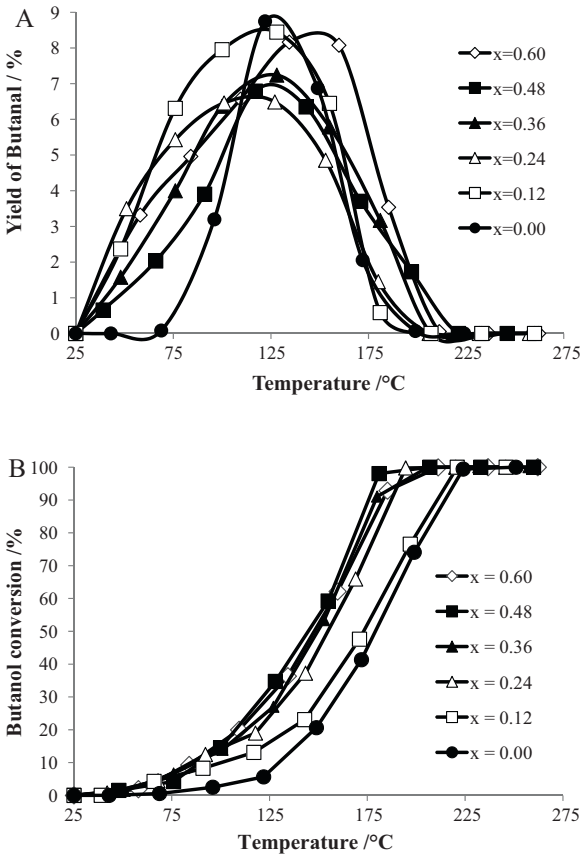

Fig. 5. Catalytic results in butanol oxidation (A) yield of butanal (%) and (B) butanol conversion (%) as a function of reaction temperature.

The single carbon-containing product of butanol oxidation is CO_2 at high conversion levels. Butanal is the major intermediate product in the course of butanol oxidation towards CO_2, other aldehydes such as propanal and ethanal are detected but in negligible concentrations. Fig. 5A presents the conversion of butanol to butanal over $Zr_{0.4}Ce_{0.6-x}Mn_xO_2$ catalysts. Mn addition to Zr–Ce system causes the formation of butanal at lower temperatures. Without cerium, the maximum of butanal yield is shifted to higher temperatures. These results are in line with the redox properties changes. It is well known that alcohol catalytic oxidation provides reaction intermediates such as aldehydes, ketons and acetic acids [11]. The major path appears to be the direct oxidation of butanal to CO_2; its oxidation via the acid is expected to be a minor path, because (1) no butanoic acid is detected and (2) CO_2 starts to be produced when the butanal concentration decreases. The same reaction scheme "butanol → butanal → CO_2" has already been observed during the homogeneous oxidation of 150 ppm of butanol in air [16]. The homogeneous conversion of butanol to butanal is maximized at around 260 °C whereas the maximum is lowered to 125 °C in the presence of $Zr_{0.4}Ce_{0.6-x}Mn_xO_2$ solid solutions.

Fig. 5B shows the butanol conversion over $Zr_{0.4}Ce_{0.6-x}Mn_xO_2$ catalysts as a function of reaction temperature. From $x = 0$ to $x = 0.24$, the catalytic activity increases with Mn addition. For $x \geq 0.36$, the catalytic activity is similar, indicating that the optimal composition is obtained for $Zr_{0.4}Ce_{0.24}Mn_{0.36}O_2$. For these compositions, 90% of butanol is transformed at about 175 °C (Fig. 5B). Despite the high quantity of manganese, the activity of $Zr_{0.4}Mn_{0.60}O_2$ is not the highest. This result can be correlated to the absence of Ce^{4+}/Ce^{3+} and Mn^{4+}/Mn^{3+} redox couples. Indeed the redox properties of catalysts are known to govern the catalytic activity in the total VOC oxidation [5,33]. These results can be connected with (i) the oxygen mobility and (ii) the surface Mn^{4+} concentration, both maximum for $x = 0.36$ value (Table 2). With similar space velocity (15,000 h^{-1}) and over a monolith Pt/Al_2O_3 catalyst, conversion of butanol higher than 90% was obtained in the 180–200 °C temperature range by Hermia and Vigneron [34]. With a double space velocity and over Co, Pd, Pt supported on γ alumina (the majority of commercial catalysts consists of Pt or Pd supported on alumina supports), 90% of butanol is transformed at 220, 220 and 180 °C, respectively [16]. This comparison with commercial catalysts illustrates the excellent behaviour of the $Zr_{0.4}Ce_{0.6-x}Mn_xO_2$ catalytic system for oxygenated VOC removal since n-butanol conversion of 90% is obtained at 175 °C for $x = 0.36$ value.

4. Conclusion

$Zr_{0.4}Ce_{0.6-x}Mn_xO_2$ solid solutions were successfully synthesized by a sol–gel method, characterized and tested for the total oxidation of butanol. The catalytic results were mainly explained by the textural (SSA and crystallite size), and bulk/surface properties (oxygen mobility and Mn^{4+} concentration). The presence of both Ce^{4+}/Ce^{3+} and Mn^{4+}/Mn^{3+} redox couples led to excellent catalytic activity for n-butanol complete oxidation with an activity maximum for $x = 0.36$.

Acknowledgements

The authors thank the European Community and the Region "Nord Pas de Calais" for financial supports through Interreg IV "Redugaz" and IRENI projects. The authors are also grateful to Mrs Martine Frere for assistance with the XPS analysis.

References

[1] J. Carpentier, J.-F. Lamonier, S. Siffert, E.A. Zhilinskaya, A. Aboukaïs, Characterisation of Mg/Al hydrotalcite with interlayer palladium complex for catalytic oxidation of toluene, Appl. Catal. A Gen. 234 (2002) 91–101.
[2] P. Papaefthimiou, T. Ioannides, X.E. Verykios, VOC removal: investigation of ethylacetate oxidation over supported Pt catalysts, Catal. Today 54 (1999) 81–92.
[3] F. Wyrwalski, J.-F. Lamonier, S. Siffert, A. Aboukaïs, Additional effects of cobalt precursor and zirconia support modifications for the design of efficient VOC oxidation catalysts, Appl. Catal. B: Environ. 70 (2007) 393–399.
[4] A. Gervasini, G.C. Vezzoli, V. Ragaini, VOC removal by synergic effect of combustion catalyst and ozone, Catal. Today 29 (1996) 449–455.
[5] B. Aellach, A. Ezzamarty, J. Leglise, C. Lamonier, J.-F. Lamonier, Calcium-deficient and stoichiometric hydroxyapatites promoted by cobalt for the catalytic removal of oxygenated volatile organic compounds, Catal. Lett. 135 (2010) 197–206.
[6] L. Lamaita, M.A. Peluso, J.E. Sambeth, H.J. Thomas, Synthesis and characterization of manganese oxides employed in VOCs abatement, Appl. Catal. B: Environ. 61 (2005) 114–119.
[7] J. Luo, Q. Zhang, A. Huang, S.L. Suib, Total oxidation of volatile organic compounds with hydrophobic cryptomelane-type octahedral molecular sieves, Microporous Mesoporous Mater. 35–36 (2000) 209–217.
[8] W. Xingyi, K. Qian, L. Dao, Catalytic combustion of chlorobenzene over MnO_x–CeO_2 mixed oxide catalysts, Appl. Catal. B: Environ. 86 (2009) 166–175.
[9] T. Rao, M. Shen, L. Jia, J. Hao, J. Wang, Oxidation of ethanol over Mn–Ce–O and Mn–Ce–Zr–O complex compounds synthesized by sol–gel method, Catal. Commun. 8 (2007) 1743–1747.
[10] S. Hamoudi, F. Larachi, A. Adnot, A. Sayari, Characterization of spent MnO_2/CeO_2 wet oxidation catalyst by TPO-MS, XPS, and S-SIMS, J. Catal. 185 (1999) 333–344.
[11] D. Delimaris, T. Ionnides, VOC oxidation over MnO_x–CeO_2 catalysts prepared by a combustion method, Appl. Catal. B. 84 (2008) 303–312.
[12] A.M.T. Silva, R.R.N. Marques, R.M. Quinta-Ferreira, Catalysts based in cerium oxide for wet oxidation of acrylic acid in the prevention of environmental risks, Appl. Catal. B. 47 (2004) 269–279.
[13] C.E. Hori, H. Permana, K.Y.S. Ng, A. Brenner, K. More, K.M. Rahmoeller, D. Belton, Thermal stability of oxygen storage properties in a mixed CeO_2–ZrO_2 system, Appl. Catal. B: Environ. 16 (1998) 105–117.
[14] U.S. Environmental Protection Agency's Integrated Risk Information System (IRIS), Summary on n-Butanol (71-36-3), http://www.epa.gov/iris/.
[15] G.D. Clayton, F.E. Clayton (Eds.), Patty's Industrial Hygiene and Toxicology, 2A, 2B, 2C, 2D, 2E, 2F: Toxicology, 4th ed., John Wiley & Sons Inc., New York, NY, 1993–1994, pp. 2639–2640.

[16] P. Papaefthimiou, T. Ioannides, X.E. Verykios, Combustion of non-halogenated volatile organic compounds over group VIII metal catalysts, Appl. Catal. B: Environ. 13 (1997) 175–184.
[17] P. Papaefthimiou, T. Ioannides, X.E. Verykios, Catalytic incineration of volatile organic compounds present in industrial waste streams, Appl. Therm. Eng. 18 (1998) 1005–1012.
[18] K. Everaert, J. Baeyens, Catalytic combustion of volatile organic compounds, J. Hazard. Mater. B109 (2004) 113–139.
[19] M.A. Cauqui, J.M. Rodriguez-Izquierdo, Application of the sol–gel methods to catalyst preparation, J. Non-Cryst. Solids 147–148 (1992) 724–738.
[20] P. Fornasiero, E. Fonda, R. Di Monte, G. Vlaic, J. Kaspar, M. Graziani, Relationships between structural/textural properties and redox behavior in $Ce_{0.6}Zr_{0.4}O_2$ mixed oxides, J. Catal. 187 (1999) 177–185.
[21] M. Wolcyrz, L. Kepinski, Rietveld refinement of the structure of CeOCI formed in Pd/CeO_2 catalyst: notes on the existence of a stabilized tetragonal phase of La_2O_3 in La-Pd-O system, J. Solid State Chem. 99 (1992) 409–413.
[22] G. Picasso, M. Gutiérrez, M.P. Pina, J. Herguido, Preparation and characterization of Ce–Zr and Ce–Mn based oxides for *n*-hexane combustion: Application to catalytic membrane reactors, Chem. Eng. J. 126 (2007) 119–130.
[23] H. Chen, A. Sayari, A. Adnot, F. Larachi, Composition–activity effects of Mn–Ce–O composites on phenol catalytic wet oxidation, Appl. Catal. B: Environ. 32 (2001) 195–204.
[24] L. Jia, M. Shen, J. Wang, X. Chu, J. Wang, Z. Hu, Redox behaviors and structural characteristics of $Mn_{0.1}Ce_{0.9}O_x$ and $Mn_{0.1}Ce_{0.6}Zr_{0.3}O_x$, J. Rare Earth 26 (2008) 523–527.
[25] L.F. Liotta, A. Longo, G. Pantaleo, G. Di Carlo, A. Martorana, S. Cimino, G. Russo, G. Deganello, Alumina supported $Pt(1\%)/Ce_{0.6}Zr_{0.4}O_2$ monolith: remarkable stabilization of ceria-zirconia solution towards $CeAlO_3$ formation operated by Pt under redox conditions, Appl. Catal. B: Environ. 90 (2009) 470–477.
[26] Z.-Q. Zou, M. Meng, Y.-Q. Zha, Surfactant-assisted synthesis, characterizations, and catalytic oxidation mechanisms of the mesoporous MnO_x–CeO_2 and Pd/MnO_x–CeO_2 catalysts used for CO and C_3H_8 oxidation, J. Phys. Chem. 114 (2010) 468–477.
[27] M. Machida, M. Uto, D. Kurogi, T. Kijima, MnO_x–CeO_2 binary oxides for catalytic NO_x sorption at low temperatures. sorptive removal of NOx, Chem. Mater. 12 (2000) 3158–3164.
[28] F. Larachi, J. Pierre, A. Adnot, A. Bernis, Ce 3d XPS study of composite $Ce_xMn_{1-x}O_{2-y}$ wet oxidation catalysts, Appl. Surf. Sci. 195 (2002) 236–250.
[29] B. Djurfors, J.N. Broughton, M.J. Brett, D.G. Ivey, Electrochemical oxidation of Mn/MnO films: formation of an electrochemical capacitor, Acta Mater. 53 (2005) 957–965.
[30] M. Toupin, T. Brousse, D. Bélanger, Influence of microstucture on the charge storage properties of chemically synthesized manganese dioxide, Chem. Mater. 14 (2002) 3946–3952.
[31] A. Laachir, V. Perrichon, A. Badri, J. Lamotte, E. Catherine, J.C. Lavalley, J. El Fallah, L. Hilaire, F. Le Normand, E. Quéméré, G.N. Sauvion, O. Touret, Reduction of CeO_2 by hydrogen. Magnetic susceptibility and Fourier-transform infrared, ultraviolet and X-ray photoelectron spectroscopy measurements, J. Chem. Soc., Faraday Trans. 87 (1991) 1601–1609.
[32] J.Z. Shyu, W.H. Weber, H.S. Gandhi, Surface characterization of alumina-supported ceria, J. Phys. Chem. 92 (1988) 4964–4970.
[33] F. Wyrwalski, J.-M. Giraudon, J.-F. Lamonier, Synergistic coupling of the redox properties of supports and cobalt oxide Co_3O_4 for the complete oxidation of volatile organic compounds, Catal. Lett. 137 (2010) 141–149.
[34] J. Hermia, S. Vigneron, Catalytic incineration for odour abatement and VOC destruction, Catal. Today 17 (1993) 349–358.